CHALMERS
UNIVERSITY OF TECHNOLOGY

Experimentally Verified, Fast Analytic, and Numerical Design of Superconducting Resonators in Flip-Chip Architectures

Citation for the original published paper (version of record):
Li, H., Shiri, D., Kosen, S. et al (2023). Experimentally Verified, Fast Analytic, and Numerical Design of Superconducting Resonators in
Flip-Chip Architectures. IEEE Transactions on Quantum Engineering, 4.
http://dx.doi.org/10.1109/TQE.2023.3302371

IEEE Transactions on Quantum Engineering

Received 10 May 2023; revised 20 July 2023; accepted 29 July 2023; date of publication 7 August 2023; date of current version 25 August 2023.

Digital Object Identifier 10.1109/TQE.2023.3302371

Experimentally Verified, Fast Analytic, and Numerical Design of Superconducting Resonators in Flip-Chip Architectures

HANG-XI LI[1], DARYOUSH SHIRI[1] (Senior Member, IEEE), SANDOKO KOSEN[1], MARCUS ROMMEL[1], LERT CHAYANUN[1], ANDREAS NYLANDER[1], ROBERT REHAMMAR[1], GIOVANNA TANCREDI[1], MARCO CAPUTO[2], KESTUTIS GRIGORAS[2], LEIF GRÖNBERG[2] (Life Member, IEEE), JOONAS GOVENIUS[2], AND JONAS BYLANDER[1]

[1]Department of Microtechnology and Nanoscience, Chalmers University of Technology, 412 96 Gothenburg, Sweden
[2]VTT Technical Research Centre of Finland, Ltd., QTF Centre of Excellence, FI-02044 VTT Espoo, Finland

Corresponding author: Hang-Xi Li (e-mail: hangxi@chalmers.se).

This work was supported in part by the Knut and Alice Wallenberg (KAW) Foundation through the Wallenberg Center for Quantum Technology (WACQT), in part by the EU Flagship on Quantum Technology H2020-FETFLAG-2018-03 Project under Grant 820363 OpenSuperQ, and in part by HORIZON-CL4-2022-QUANTUM-01-SGA Project under Grant 101113946 OpenSuperQPlus100.

ABSTRACT In superconducting quantum processors, the predictability of device parameters is of increasing importance as many laboratories scale up their systems to larger sizes in a 3-D-integrated architecture. In particular, the properties of superconducting resonators must be controlled well to ensure high-fidelity multiplexed readout of qubits. Here, we present a method, based on conformal mapping techniques, to predict a resonator's parameters directly from its 2-D cross-section, without computationally heavy and time-consuming 3-D simulation. We demonstrate the method's validity by comparing the calculated resonator frequency and coupling quality factor with those obtained through 3-D finite-element-method simulation and by measurement of 15 resonators in a flip-chip-integrated architecture. We achieve a discrepancy of less than 2% between designed and measured frequencies for 6-GHz resonators. We also propose a design method that reduces the sensitivity of the resonant frequency to variations in the interchip spacing.

INDEX TERMS Conformal mapping, coplanar waveguide (CPW), flip chip, kinetic inductance (KI), penetration depth, quantum processor, superconducting resonator.

I. INTRODUCTION

As the size of superconducting quantum processors grows beyond a small number of qubits, more advanced circuit-integration technology needs to be developed to accommodate the increasing input/output (I/O) wiring complexity. To this end, flip-chip integration is one choice that allows the routing of individual I/O lines to address qubits in the interior of the processor [1], [2], [3]. Flip-chip integration technology has been demonstrated to be compatible with high-quality qubits [3], [4], [5], [6], [7], [8], [9]. Flip-chip modules comprise two or more dies that have been aligned and bonded together—in the minimal version using a "qubit" tier and a "control" or "interposer" tier, separating the fabrication of qubits and I/O circuitry onto different tiers. To achieve high-performance qubit control and readout, the measured resonant frequencies and other device parameters must agree with their design targets. The electromagnetic analytic and numerical design methodology also needs to be efficient, since 3-D electromagnetic modeling of the full circuit is computationally intensive. A conventional simulation strategy is to sweep multiple design parameters of the resonator geometry to meet target f_r and Q_c values [5]. While this is appropriate for small devices, scaling it beyond a few resonators becomes too time-consuming.

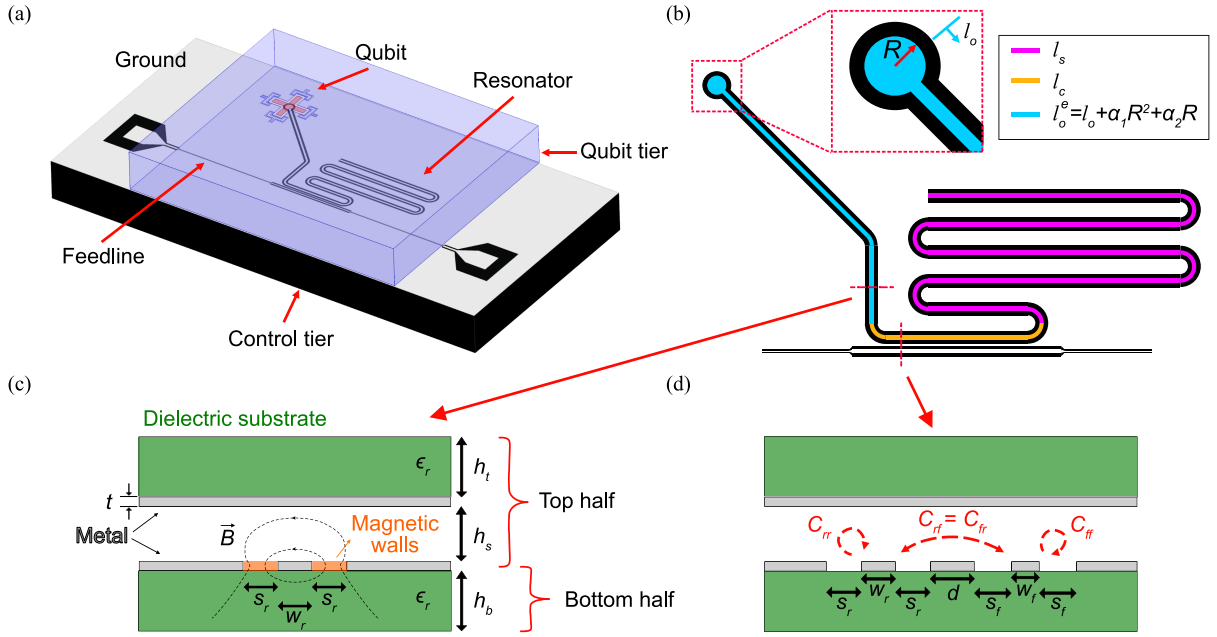

FIGURE 1. (a) False-color 3-D model of a $\lambda/4$ resonator coupled to a feedline, on the control tier (Bottom), facing a metal ground plane on the qubit tier (Top) with a qubit located opposite from the open end of the resonator. (b) Top view of the resonator design. The resonator can be separated into three parts: 1) effective open part l_o^e (cyan), 2) coupling part l_c (yellow), and 3) short part l_s (pink). The effective open part contains both an open part l_o and an effective length ($\alpha_1 R^2 + \alpha_2 R$) due to the circular coupling structure. All the gap areas (black) of the resonator, including the circular coupling structure at the open end, have the same distance to the ground plane. (c) Cross section of the resonator's CPW. The top and bottom halves of the cross section, separated by the metal surface of the control tier (Bottom), can be independently transformed into two parallel plates, using conformal mapping techniques, when the magnetic walls (orange) are placed on the surfaces of the CPWs gap area. (d) Cross section of the resonator's coupling part with the feedline. The capacitance between the resonator's and the feedline's center conductors ($C_{rf} = C_{fr}$) and their self-capacitances (C_{rr}, C_{ff}) are simulated to obtain the coupling quality factor Q_c to the feedline.

In this article, we present a design methodology for superconducting flip-chip-integrated quantum processor components. We apply it to the calculation of resonant frequencies (f_r) of coplanar-waveguide (CPW) resonators and their coupling quality factors to a readout feedline (Q_c). By analyzing only the 2-D cross-section of the CPW, we calculate these quantities using two methods: 1) conformal mapping analysis; and 2) 2-D numerical simulation. We compare the results to those obtained by 1000 times more resource-demanding 3-D simulation and to experimental measurements of 15 aluminum resonators in a flip-chip quantum processor architecture. With the inclusion of the kinetic inductance (KI) contribution, we predict the resonant frequencies with accuracy better than 100 MHz.

The interchip spacing can be off-target or may vary across a flip-chip module. For a resonator that faces a ground plane on the opposing chip, we propose a design method with a partial ground-plane cutout of the area directly facing the resonator, reducing the sensitivity of its resonant frequency to the interchip spacing.

II. 2-D CROSS-SECTIONAL CALCULATIONS

In this section, we show the calculation of f_r and Q_c from a CPW resonator's 2-D cross-sections in flip-chip geometry with an interchip vacuum gap. Fig. 1(a) shows a 3-D model of a typical quarter-wavelength ($\lambda/4$) resonator resting on the control tier, coupled to a feedline, also on the control tier, and to a qubit on the opposing qubit tier. We focus on the typical scenario in which the whole CPW resonator and feedline are facing a metal ground plane on the qubit tier [1], [5].

A. RESONANT FREQUENCY

The resonant frequency of a $\lambda/4$ resonator is calculated by

$$f_r = \frac{1}{4 l_{\text{tot}} \sqrt{(L_l^g + L_l^k) \cdot C_l}} \tag{1}$$

where l_{tot} is its total length including the effective lengths resulting from CPW discontinuities at both ends. L_l^g and L_l^k are the geometric and KIs per unit length, respectively, and C_l is the capacitance per unit length.

We can obtain L_l^g and C_l by using either conformal mapping techniques ($L_l^{g,\text{conf}}$, C_l^{conf}) [10] or 2-D finite-element-method (FEM) simulation ($L_l^{g,\text{sim2D}}$, C_l^{sim2D}) [11] of the resonator's CPW cross-section, as illustrated in Fig. 1(c). Here, $h_b = h_t$ represent the substrate thicknesses of the control and qubit tiers, h_s is the interchip spacing, and w_r and s_r are the width and gap of the CPW line, respectively. We will examine the accuracies of calculations of f_r using both 2-D approaches.

To implement the conformal mapping techniques, we assume that the metal thin films of the resonator's central

conductor and of the ground planes on both tiers have infinite conductivity and that the CPW cross-section satisfies the quasi-TEM approximation. In order to simplify the conformal transformation functions, the metal thin films are assumed to have zero thickness ($t = 0$), and two magnetic walls are placed on the dielectric–vacuum interfaces, i.e., the gaps of the CPW, assuming that the magnetic field is perpendicular to the vacuum-dielectric interfaces [12]. As shown in Fig. 1(c), the resonator's cross-section can then be separated into two independent halves (top and bottom) by the metal surface of the control tier, from which different conformal mapping techniques are applied to the two halves. This results in parallel-plate waveguides with different widths and separations, see Appendix A.

The total $L_l^{g,\mathrm{conf}}$ and C_l^{conf} values are, therefore, calculated as the parallel combination of the two halves. We have [12], [13]

$$L_l^{g,\mathrm{conf}} = \left(1/L_l^{g,t} + 1/L_l^{g,b}\right)^{-1} = \frac{\mu_0}{2}\left[\frac{K(k_s)}{K(k_s')} + \frac{K(k_1)}{K(k_1')}\right]^{-1} \tag{2}$$

$$\begin{aligned} C_l^{\mathrm{conf}} &= C_l^t + C_l^b \\ &= 2\varepsilon_0 \frac{K(k_s)}{K(k_s')} + 2\varepsilon_0\left[\frac{K(k_1)}{K(k_1')} + (\varepsilon_r - 1)\frac{K(k_2)}{K(k_2')}\right] \end{aligned} \tag{3}$$

where t and b represent the top and bottom halves of the CPW cross-section, respectively. Here, μ_0 is the vacuum permeability, ε_0 is the vacuum permittivity, ε_r is the relative permittivity of the substrate of both tiers, and $K(k)$ is the complete elliptic integral of the first kind with modules

$$k_1 = \frac{w_r}{w_r + 2s_r} \tag{4}$$

$$k_2 = \sinh\left[\frac{\pi w_r}{4h_b}\right] / \sinh\left[\frac{\pi (w_r + 2s_r)}{4h_b}\right] \tag{5}$$

$$k_s = \tanh\left[\frac{\pi w_r}{4h_s}\right] / \tanh\left[\frac{\pi (w_r + 2s_r)}{4h_s}\right] \tag{6}$$

$$k_i' = \sqrt{1 - k_i^2} \ (i = 1, 2, s). \tag{7}$$

A detailed derivation of (2)–(3) is shown in Appendix A.

We then compare $L_l^{g,\mathrm{conf}}$ and C_l^{conf} obtained by conformal mapping techniques with 2-D FEM simulation under different interchip spacings h_s. We use $h_b = h_t = 280\,\mu$m, and $\varepsilon_r = 11.45$ for our high-resistivity silicon substrate of both tiers at cryogenic temperature [14]. We approximate our aluminum superconducting films ($t = 150$ nm) using finite-thickness perfect conductors during the 2-D FEM simulation. We use $w_r = s_r = 12\,\mu$m for the resonator's CPW geometry.

As shown in Fig. 2(a) and (b), when h_s is small, L_l^g and C_l are heavily influenced by the top half-part of the cross section, governed by the factor $K(k_s)/K(k_s')$ in (2) and (3). When h_s increases (the opposing ground plane is moving away from the CPW resonator), its influence decreases and both

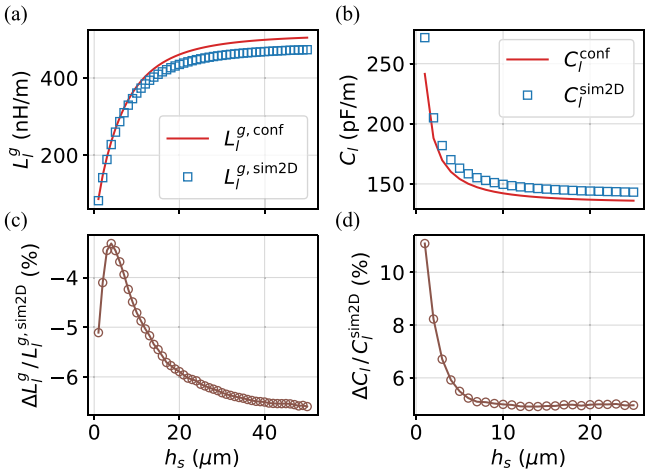

FIGURE 2. (a) Geometric inductance per unit length L_l^g and (b) capacitance per unit length C_l of the resonator's CPW cross-section obtained by conformal mapping calculation and 2-D FEM simulation, respectively, under different interchip spacings h_s. (c) and (d) Their differences $\Delta L_l^g = L_l^{g,\mathrm{sim2D}} - L_l^{g,\mathrm{conf}}$ and $\Delta C_l = C_l^{\mathrm{sim2D}} - C_l^{\mathrm{conf}}$.

conformal-mapping values and simulated values approach a limit as if the ground plane was absent ($h_s = \infty$).

For comparison between the conformal mapping technique and 2-D FEM simulation, we calculate $\Delta L_l^g = L_l^{g,\mathrm{sim2D}} - L_l^{g,\mathrm{conf}}$ and $\Delta C_l = C_l^{\mathrm{sim2D}} - C_l^{\mathrm{conf}}$ for each h_s, as shown in Fig. 2(c) and (d). We find that $\Delta L_l^g / L_l^{g,\mathrm{sim2D}}$ and $\Delta C_l / C_l^{\mathrm{sim2D}}$ stabilize at around -7% and 5%, respectively, for large h_s. This difference can be understood as the error of the zero-thickness assumption of the metal thin film, which is used during the conformal mapping transformation, compared with 2-D FEM simulations which consider the edge effect of finite-thickness thin films [15]. When $h_s \leq 4\,\mu$m, the invalidity of the introduced magnetic wall on the resonator gap areas during conformal-mapping calculations is clearly shown, as $\Delta L_l^g / L_l^{g,\mathrm{sim2D}}$ and $\Delta C_l / C_l^{\mathrm{sim2D}}$ increase rapidly with smaller h_s. The cross section of the CPW resonator in the flip-chip geometry, therefore, needs to be considered as a whole when h_s is very small, rather than being separated into two halves and treated independently.

Having determined L_l^g and C_l, we also need to know the KI to calculate f_r. It is given by [16], [17]

$$L_l^k = \frac{\mu_0 \lambda_m^2}{|I|^2} \cdot \int J_z^2 \, dS \tag{8}$$

where J_z is the supercurrent density in the direction of the current flow, and the surface integral is over the cross section of the thin film only. For a flip-chip geometry, the integral also includes the qubit tier's metal ground plane. Furthermore, λ_m is the magnetic penetration depth of the superconductor, and I is the total current injected into the CPWs center conductor.

To calculate (8), we need to know λ_m and J_z over the whole thin-film cross-section. We determine J_z by electromagnetic simulation as in [18]. In order to circumvent the complexity

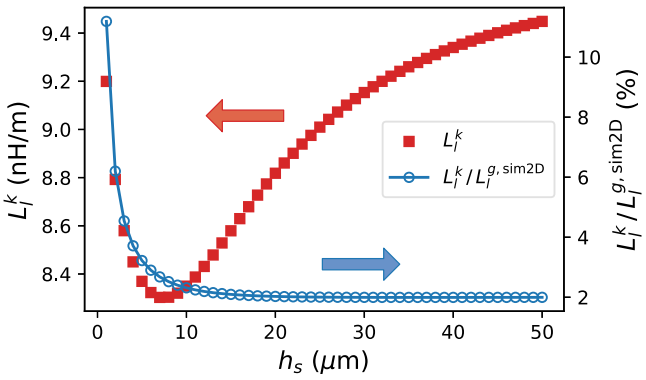

FIGURE 3. Simulated KI per unit length L_l^k and its ratio to the simulated geometric inductance per unit length $L_l^{g,\mathrm{sim2D}}$ under different interchip spacings h_s. We use a magnetic penetration depth $\lambda_m = 83$ nm for the superconducting thin films during the simulation.

of evaluating λ_m of a deposited aluminum thin film [19], [20], [21], [22], [23], we directly compare measured resonant frequencies of six single-chip resonators with their simulated values and obtain a fitted $\lambda_m = 83$ nm, assuming the average frequency discrepancy between measurement and simulation is due to the omission of the KI during the simulations. More details of the method to extract λ_m are described in Appendix B.

Fig. 3 shows L_l^k and its ratio to $L_l^{g,\mathrm{sim2D}}$ under different h_s. Notice that L_l^k has a minimum around $h_s = 7\,\mu$m. As the surface integral is on J_z^2, both the injected current on the center conductor and the return current on both tiers' ground planes contribute to L_l^k. The simulated distribution of J_z shows that when h_s is small, the return current concentrates on the qubit tier's metal directly facing the resonator's central conductor, and when h_s is large, most of J_z flows on the edges of the control tier's CPW structure [17], [18]. When h_s is at around $7\,\mu$m, the distribution of J_z is in-between the two extremes and has permeated the largest cross-sectional area of the thin film.

B. COUPLING QUALITY FACTOR

The coupling quality factor Q_c of the resonator quantifies its coupling rate to the feedline, determining how fast the qubit state can be detected [24]. In addition, coupling to the feedline changes the resonator's characteristic impedance in the coupling area and causes a frequency shift δf_r^c [25].

We use conformal mapping results [25] to calculate the resonator's Q_c and δf_r^c. Assuming the characteristic impedance of the feedline matches the I/O port (50 Ω), we have

$$\frac{1}{Q_c} = \frac{2\kappa^2 \sin^2\theta}{\pi(2p-1)} \tag{9}$$

$$\delta f_r^c = -\frac{c_l \sin\theta}{2\pi l_{tot}} \cdot \left[\frac{\kappa^2(2\cos\psi + \cos\theta)}{2} + \frac{(Z_2 - Z_r)\cos\psi}{Z_r}\right] \tag{10}$$

with

$$\kappa = -C_{rf}/\sqrt{C_{rr}C_{ff}} \tag{11}$$

$$c_l = f_r \cdot 4l_{\mathrm{tot}} \tag{12}$$

$$Z_2 = 1/\left(c_l C_{ff}\sqrt{1-\kappa^2}\right) \tag{13}$$

$$\theta = 2\pi l_c/(4l_{\mathrm{tot}}) \tag{14}$$

$$\psi = 2\pi(l_c + 2l_o^e)/(4l_{\mathrm{tot}}) \tag{15}$$

where f_r is the bare resonator frequency without feedline, and we take $p = 1$ for its fundamental resonance. As shown in Fig. 1(b), l_c is the length of the coupling part between resonator and feedline, including two additional 90° arcs at both ends of the coupling part to take into account the spurious coupling [25]; l_o^e is the effective length of the open part of the resonator, including the effective length of the coupling structure to the qubit; Z_r is the characteristic impedance of the resonator; and c_l is the speed of light within the resonator's CPW cross-section. The coupling capacitance ratio κ and the impedance Z_2 of the resonator's coupling part are calculated from the capacitance between the resonator's and the feedline's center conductors C_{rf}, and their self-capacitances (C_{rr}, C_{ff}).

In order to obtain precise values of C_{rf}, C_{rr}, and C_{ff} under different h_s, we conduct 2-D FEM simulations at the cross section of the resonator's coupling part to the feedline. Fig. 1(d) shows the cross section of the resonator's coupling area where its center conductor is in parallel with the feedline.

III. COMPARISON WITH 3-D FEM SIMULATION

To validate the accuracy of the resonator's f_r and Q_c obtained from 2-D cross-sections, both parameters are compared to 3-D FEM simulation [26] of a resonator as shown in Fig. 1(a) with $(l_s, l_c, l_o) = (3780.3,\ 425.7,\ 850.4)\,\mu$m, where l_s is the short part and l_o is the open part of the resonator up to the center of the circular structure for qubit-resonator coupling. The circular structure has inner radius $R = 29.4\,\mu$m. Here, L_l^k is not included during the f_r calculation in this comparison, because a perfect-E boundary condition on the 2-D zero-thickness sheets is used during the 3-D FEM simulations to approximate the superconducting thin films [5]. We use $w_f = 9\,\mu$m and $s_f = 10\,\mu$m for the feedline's CPW geometry with the coupling gap $d = 6\,\mu$m during the Q_c calculation.

To obtain a precise value of l_{tot} in (1), in addition to the resonator's designed length $l_r = l_s + l_c + l_o$, we also need to estimate the effective length of the circular structure at the open end of the resonator. We introduce two empirical coefficients (α_1, α_2) so that $l_{\mathrm{tot}} = l_r + \alpha_1 R^2 + \alpha_2 R$. These coefficients are obtained by sweeping R at a fixed h_s and fitted with f_r from 3-D simulations. We obtain $\alpha_1 = 0.032\,\mu\mathrm{m}^{-1}$ and $\alpha_2 = 2.9$. We disregard the small effective length of the short end of the resonator [27]. More details are found in Appendix C.

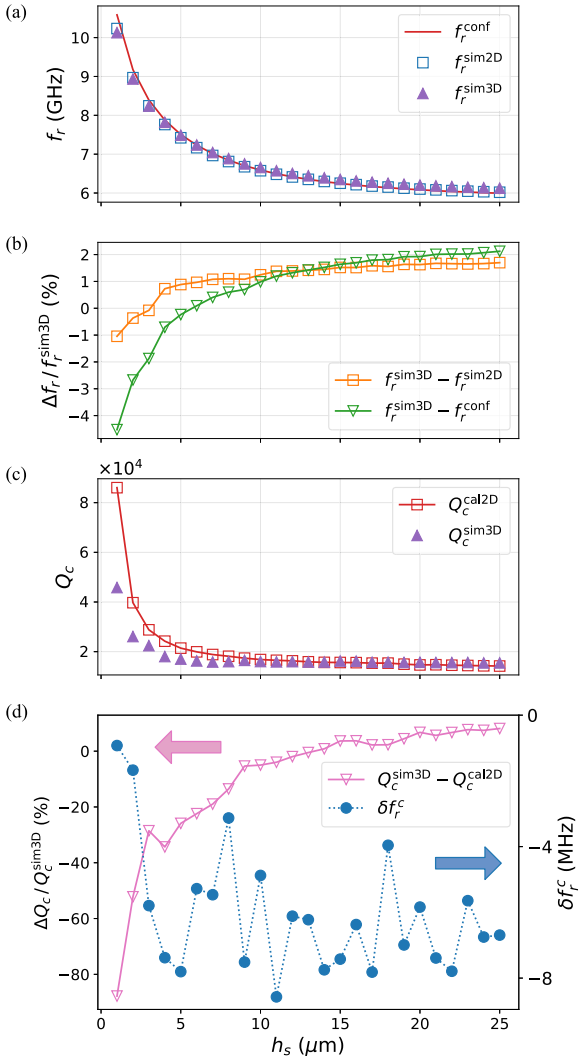

FIGURE 4. (a) Resonator frequencies obtained from conformal mapping calculation f_r^{conf}, 2-D FEM simulation f_r^{sim2D}, and 3-D FEM simulation f_r^{sim3D} under different interchip spacings h_s. (b) Frequency difference Δf_r between 3-D and 2-D FEM simulation, and between 3-D FEM simulation and conformal mapping calculation. (c) Resonator coupling quality factor obtained from 2-D cross-sections Q_c^{cal2D} and 3-D FEM simulation Q_c^{sim3D} and (d) their difference, together with the coupling-induced frequency shift δf_r^c under different h_s. δf_r^c is calculated using f_r^{sim2D} for the bare resonator frequency.

Fig. 4(a) and (b) shows the comparison between f_r obtained by 3-D FEM simulations (f_r^{sim3D}), 2-D FEM simulations (f_r^{sim2D}), and conformal mapping techniques (f_r^{conf}) under different h_s values. The cross-sectional calculations, f_r^{sim2D} and f_r^{conf}, were calculated from their L_l^g and C_l values, with δf_r^c added. In particular, f_r^{sim2D} and f_r^{sim3D} differ by 2% over the whole h_s range, and f_r^{conf} is similarly accurate when $h_s \geq 3\,\mu$m.

Considering a typical readout resonator with $f_r = 6$ GHz, we, therefore, expect less than 100-MHz error between frequencies obtained by 2-D cross-section and 3-D FEM simulation. This error is acceptable in typical multiplexing readout situations [28], [29]. The benefit of the 2-D cross-sectional method is that it substantially reduces the simulation time and required computer memory when designing resonators over a parameter split, or in large circuits. We show the comparison of required computational resources between 3-D FEM simulation and 2-D FEM simulation in Appendix D—in our case, a factor of 1000. Furthermore, conformal-mapping techniques require only analytical calculations, reducing the need for extensive computational resources.

Fig. 4(c) and (d) also shows a difference of less than 20% between Q_c^{cal2D}, obtained from a 2-D cross-section, and that from 3-D FEM simulation, Q_c^{sim3D}, when $h_s \geq 7\,\mu$m. When h_s is smaller than 7 μm, the feedline may become less well matched to the I/O port.

IV. COMPARISON WITH MEASUREMENT

We now examine our 2-D cross-sectional techniques by calculating the resonant frequencies and coupling quality factors of 15 resonators by means of conformal transformation and 2-D FEM simulation, $f_r^{conf+KI}$, $f_r^{sim2D+KI}$, and Q_c^{cal2D} (including simulated KI L_l^k), and comparing them with experimentally measured values. The resonators were fabricated and packaged within a multiqubit flip-chip-integrated quantum processor as reported by Kosen and Li [5]. They were measured at millikelvin temperature, and their parameters f_r^{meas} and Q_c^{meas} were determined from the forward transmission scattering parameter S_{21} in the high-power regime, where these resonators are decoupled from their corresponding qubits [30].

To obtain the value of h_s for each of the 15 resonators within one flip-chip-integrated processor, we used the gap values, measured by scanning electron microscopy, at the chip's four corners [5] and inferred the tilt of the interchip distance using bilinear interpolation (assuming flat surfaces). Fig. 5(a) shows the locations of the 15 resonators.

Fig. 5(b) shows a comparison between the calculated and measured f_r of these 15 resonators. Here $f_r^{conf+KI}$ and $f_r^{sim2D+KI}$ deviate from the measured frequencies (f_r^{meas}) by less than 2%, demonstrating the accuracy of our 2-D cross-sectional calculation method. The inclusion of the KI has shifted up these frequency differences by about 1.2%, resulting in a deviation between f_r^{meas} and $f_r^{sim3D+KI}$ to be around 0%. We observe the monotonic change of the frequency differences at each row of resonators, indicating that there is a residual chip tilt that has not been compensated by the bilinear interpolation of the interchip distance from the chip's four corners.

Fig. 5(c) shows that across 15 resonators, Q_c^{cal2D} and Q_c^{sim3D} are kept at certain values, as all resonators' coupling lengths l_c and coupling gaps d are designed to be the same. Q_c^{cal2D} and Q_c^{sim3D} differ by around 13%, cf. Fig. 4(c) for $h_s \sim 8\,\mu$m. The measured coupling quality factors Q_c^{meas} oscillate across 15 resonators, resulting in deviation from -20% to $+10\%$ to either Q_c^{cal2D} or Q_c^{sim3D}. We attribute such oscillation to impedance mismatch between feedline and I/O port at wire-bond interconnections to the printed circuit board.

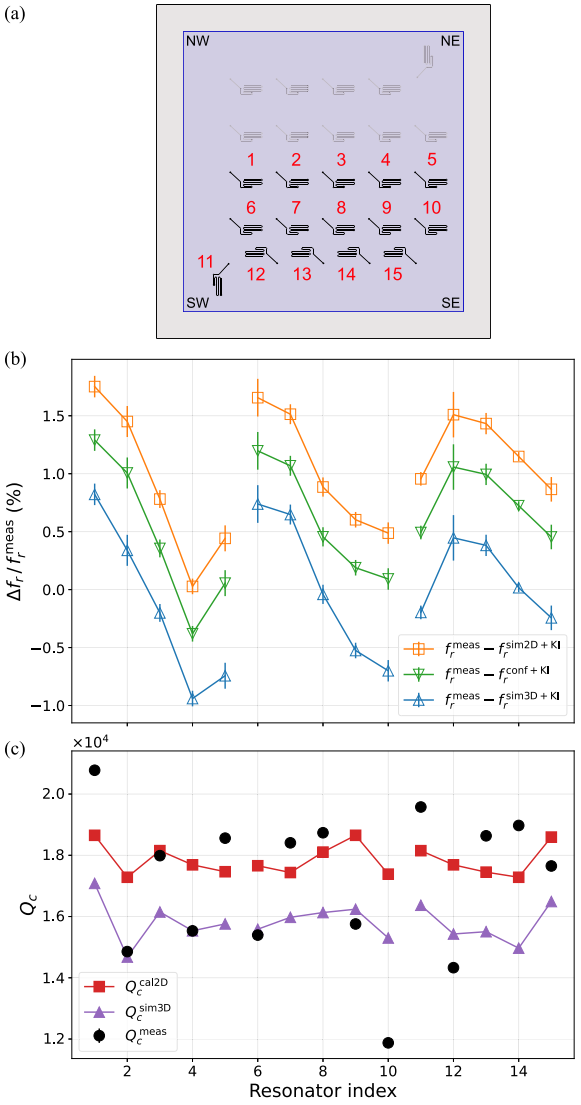

FIGURE 5. Comparison between 2-D cross-sectional calculation and measurement results of 15 resonators within a flip-chip quantum processor. (a) Illustration of the positions of 15 resonators within the processor. Gap measurement by scanning electron microscopy at the processor's four corners yielded [NW, NE, SW, SE] = [8.3, 9.3, 8.3, 8.8] μm. (b) Frequency difference between measurements f_r^{meas}, conformal mapping calculations $f_r^{\text{conf+KI}}$, 2-D FEM simulations $f_r^{\text{sim2D+KI}}$, and 3-D FEM simulations $f_r^{\text{sim3D+KI}}$, including KI. (c) Coupling quality factor obtained from measurements Q_c^{meas}, 2-D cross-sectional calculations Q_c^{cal2D}, and 3-D FEM simulations Q_c^{sim3D}.

V. INTERCHIP-SPACING INSENSITIVE FLIP-CHIP RESONATOR DESIGN

In Fig. 4(a), we see that the resonator frequency f_r is sensitive to the change of interchip spacing h_s, especially when h_s is below 10 μm, where 1 μm variation of h_s can result in larger than 100 MHz change of f_r. We note that the rapid increase of f_r for decreasing h_s is due to a rapid decrease of L_l^g. In this section, we propose a method to reduce the sensitivity of f_r to h_s by partly removing the metal ground plane facing the CPW resonator on the opposing chip. We first use conformal transformation to determine $L_l^{g'}$ and C_l' of the resonator's cross-section in the case where no metal

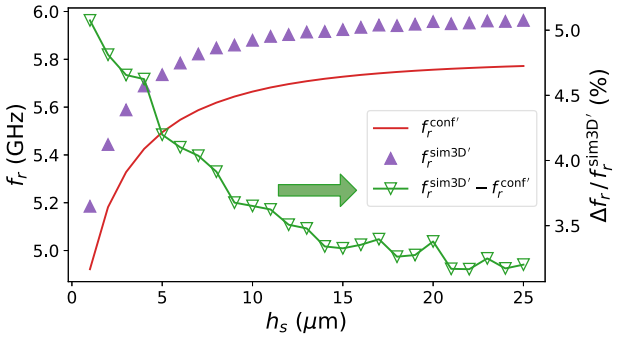

FIGURE 6. Resonator frequencies obtained from conformal mapping calculation $f_r^{\text{conf}'}$ and 3D FEM simulation $f_r^{\text{sim3D}'}$ under different inter-chip spacings h_s when the resonator's CPW line is facing a dielectric substrate on the opposing chip, together with the frequency difference between 3-D FEM simulation and conformal mapping calculation.

is facing the CPW line, i.e., the CPW line is directly facing the dielectric substrate of the qubit tier. We then calculate the optimal ratio between the resonator's dielectric-facing length to its total length, such that at a certain range of h_s, the sensitivity of f_r to h_s is minimized.

A. RESONATOR CPW FACING DIELECTRIC

We use conformal mapping techniques to obtain $L_l^{g,\text{conf}'}$ and $C_l^{\text{conf}'}$ of the cross section when the CPW resonator faces the dielectric substrate of the opposing chip. The resulting equations are

$$L_l^{g,\text{conf}'} = \frac{\mu_0}{4}\frac{K(k_1')}{K(k_1)} \tag{16}$$

$$C_l^{\text{conf}'} = \frac{2\varepsilon_0}{\left(\varepsilon_r \frac{K(k_1)}{K(k_1')}\right)^{-1} + \left(\frac{\varepsilon_r}{\varepsilon_r - 1}\frac{K(k_s)}{K(k_s')}\right)^{-1}} + 2\varepsilon_0\left[\frac{K(k_1)}{K(k_1')} + (\varepsilon_r - 1)\frac{K(k_2)}{K(k_2')}\right]. \tag{17}$$

To derive the capacitance per unit length, as in Appendix A, we separate the capacitance contribution of the vacuum from that of the qubit tier's substrate at the top half of the cross section. However, since the CPW metal is closer to the inter-chip vacuum than the qubit tier's substrate, their capacitance contributions are taken in series rather than in parallel [31].

Fig. 6 shows $f_r^{\text{conf}'}$ and $f_r^{\text{sim3D}'}$ when the resonator's CPW line faces the dielectric. $f_r^{\text{sim3D}'}$ is obtained using the same resonator as in Section III, but with the entire metal film removed from the opposing chip. $f_r^{\text{conf}'}$ is calculated using $L_l^{g,\text{conf}'}$ and $C_l^{\text{conf}'}$, with an added coupling-induced frequency shift: It gives quantitatively the same result as $f_r^{\text{sim3D}'}$, differing by 3% to 5.5% under different h_s.

Using the same participation ratio simulation setting as in [5], we also simulate the participation ratio of lossy dielectric interfaces and compare the resulting Q-factors of the resonator's cross-section when the CPW line faces either a metal or a dielectric. See Appendix E for details.

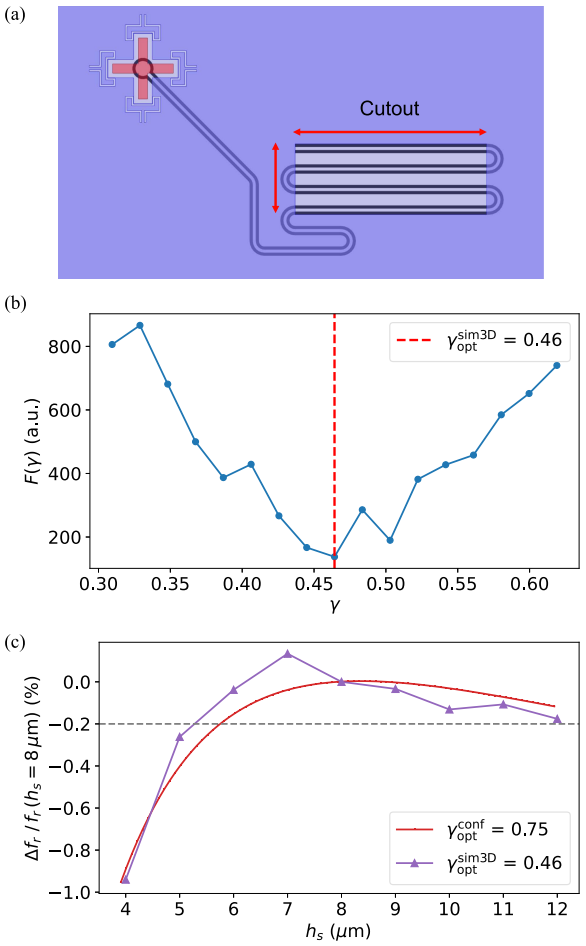

FIGURE 7. (a) Illustration of a $\lambda/4$ resonator facing a partial cutout of the metal ground plane on the opposing chip. (b) Cost function $F(\gamma)$ calculated from 3-D FEM simulations of the resonator with $(h_s^N - h_s^1)/N = 1\,\mu$m. The optimal coverage ratio $\gamma_{opt}^{sim3D} = 0.46$ is found at the minimum of $F(\gamma)$. (c) Resonator frequency variation around $h_s = 8\,\mu$m for $\gamma = \gamma_{opt}$, obtained from conformal mapping calculation and 3-D FEM simulation, respectively.

B. GROUND-PLANE CUTOUT TO REDUCE THE FREQUENCY DEPENDENCE ON INTERCHIP-SPACING

Since in these two scenarios (CPW facing either metal or dielectric, cf. Figs. 4(a) and 6), the resonator's f_r exhibits the opposite response to a change of interchip spacing h_s, we can use this to render f_r insensitive to small h_s variations around a chosen value within our typical range $6\,\mu\text{m} < h_s < 10\,\mu\text{m}$ [5].

We define γ as the ratio between the resonator length facing dielectric substrate and the resonator's total length l_{tot}. We can approximate the effective inductance and capacitance per unit length as

$$L_l^e = (1-\gamma)(L_l^{g,\text{conf}} + L_l^k) + \gamma(L_l^{g,\text{conf}'} + L_l^{k'}) \tag{18}$$

$$C_l^e = (1-\gamma)C_l^{\text{conf}} + \gamma C_l^{\text{conf}'} \tag{19}$$

where $L_l^{k'}$ is the KI per unit length when the CPW faces dielectric.

To find the optimal value γ_{opt} of minimal sensitivity to h_s variation, we use a cost function $F(\gamma)$ independent of the total length

$$F(\gamma) = \sum_{i=1}^{N} \left| \frac{\partial (L_l^e C_l^e)^{-1/2}}{\partial h_s^i} \right| \tag{20}$$

where $h_s^i = h_s^1 + (i-1)(h_s^N - h_s^1)/N$ with $N \in \mathbb{N}^*$, and γ_{opt} is the value that minimizes $F(\gamma_{\text{opt}})$ in the range $h_s \in [h_s^1, h_s^N]$.

We obtain $\gamma_{\text{opt}}^{\text{conf}} = 0.75$ for $h_s \in [6, 10]\,\mu$m for large enough N. We ignore the KI during the calculation, using the fact that at large h_s, $L_l^{g,\text{conf}} = L_l^{g,\text{conf}'}$ and $L_l^k = L_l^{k'}$, and when $h_s \geq 6\,\mu$m, $L_l^k / L_l^{g,\text{conf}} \approx L_l^{k'} / L_l^{g,\text{conf}'}$ (see Fig. 3). As shown in Fig. 7(c), the deviation of f_r from its value at $h_s = 8\,\mu$m, within this range, can be less than 0.2%.

We employ this principle to the actual resonator design as in Fig. 1 to validate our calculation. For simplicity, we cut out a rectangular area on the opposing chip's metal ground plane, so that part of the resonator's CPW line faces the substrate, as shown in Fig. 7(a). We found that $\gamma_{\text{opt}}^{\text{sim3D}} = 0.46$ for the actual resonator and obtained a similar deviation of f_r around $h_s = 8\,\mu$m as the calculation [see Fig. 7(b) and (c)]. We attribute the discrepancy between $\gamma_{\text{opt}}^{\text{conf}}$ and $\gamma_{\text{opt}}^{\text{sim3D}}$ to the meandering structure of the resonator, supported by the additional simulation result that $\gamma_{\text{opt}}^{\text{sim3D}} = \gamma_{\text{opt}}^{\text{conf}}$ if the resonator is realized by a straight CPW line instead.

VI. CONCLUSION

In conclusion, we have shown that analytic and numerical simulation of a 2-D cross-section of a CPW superconducting resonator in flip-chip geometry can predict the resonant frequency within 2% of 3-D-simulated and measured values, after considering the effective length correction due to the resonator ends. We also determined the coupling quality factor within 20% by 2-D simulation.

The 2-D cross-sectional method is considerably more computationally efficient than conventional 3-D FEM simulations. The three orders of magnitude speed-up will become particularly useful for large-scale quantum processor design containing a large number of qubits and resonators. The conformal mapping analytic equations and 2-D simulation steps can be easily integrated into the process design kit workflow of superconducting quantum processor design, e.g., using newly developed tools like Qiskit Metal. This method can also be generalized to other components implemented using CPW transmission lines, e.g., couplers and Purcell filters.

In addition, we have proposed a resonator design that is insensitive to interchip-spacing variations.

APPENDIX A
CONFORMAL TRANSFORMATIONS FOR FLIP-CHIP CPW CROSS-SECTION

In this appendix, we will use conformal mapping techniques to derive the geometric inductance and capacitance per unit length of the CPW cross-section in flip-chip geometry when

the CPW line faces a metal ground plane on the opposing chip.

To simplify our conformal transformation functions such that they are feasible to calculate analytically, we assume zero thickness of the metal thin films on both tiers. We also assume that the interchip spacing h_s is large enough, such that the magnetic field around the CPW center conductor is perpendicular to the vacuum–dielectric interfaces at gap areas of the CPW. We are then able to cover the vacuum–dielectric interfaces with magnetic walls and separate the CPW cross-section into two halves. See Fig. 1(c).

We then apply conformal transformations to the separated two halves independently, resulting in different parallel-plate waveguides with different widths W and separations H. The geometric inductance and capacitance per unit length of each parallel-plate waveguide are therefore calculated using

$$L_l^g = \mu_0 \frac{H}{W} \tag{21}$$

$$C_l = \varepsilon_r^p \varepsilon_0 \frac{W}{H} \tag{22}$$

where ε_r^p is the relative permittivity of the dielectric medium between two plates after the conformal transformation. We use different conformal mapping techniques for each half. The contributions of two halves to the total geometric inductance and capacitance per unit length of the CPW cross-section are calculated as a parallel combination.

A. BOTTOM HALF

Now we will show how to do the conformal transformation to each half of the cross section. We start with the bottom half in Fig. 1(c). This half can be seen as a conventional CPW cross-section having a dielectric substrate with relative permittivity ε_r.

We first calculate the geometric inductance per unit length of the bottom-half cross-section. We replace the substrate with the vacuum since their permeability are the same. We first put the cross section into a complex z-plane. Because all the metals are in the horizontal direction, we can put the metals along with the Re[z]-axis and directly apply the Christoffel–Schwartz transformation [10] to conformally map these metals into a parallel-plate waveguide [32] in the complex w-plane. The transformation function we use is

$$w(z) = A_1 \int_0^z \frac{dz}{\sqrt{(z - z_B)(z - z_C)(z - z_D)(z - z_E)}} + A_2. \tag{23}$$

Here, A_1 and A_2 are constants that determine the scaling and translation of the transformed geometry, and $z_i\,(i = B, C, D, E)$ are the positions of the end points of the metals on the Re[z]-axis. Choosing the center of the CPWs center conductor as the zero position of the Re[z]-axis, we have $-z_B = z_E = (w_r + 2s_r)/2$ and $-z_C = z_D = w_r/2$.

The geometry in the z-plane is now conformally mapped to the w-plane. As a result, the CPW center conductor and the ground plane (two infinite points viewed as connected) in the z-plane are transformed into the two plates with equal width and separated in parallel, forming a parallel-plate waveguide with a vacuum in-between the plates.

The width and the height of this parallel-plate waveguide are calculated as

$$W_b^{\text{vac}} = |w_D - w_C| = |A_1| 2K(k_1) \tag{24}$$

$$H_b^{\text{vac}} = |w_E - w_D| = |A_1| K(k_1') \tag{25}$$

where $K(k)$ is the complete elliptic integral of the first kind with modules $k_1 = z_D/z_E = w_r/(w_r + 2s_r)$ and $k_1' = \sqrt{(1 - k_1^2)}$.

The geometric inductance per unit length of this parallel-plate waveguide is obtained as

$$L_l^{g,b} = \mu_0 \frac{H_b^{\text{vac}}}{W_b^{\text{vac}}} = \frac{\mu_0}{2} \frac{K(k_1')}{K(k_1)}. \tag{26}$$

To calculate the capacitance per unit length of the bottom-half cross-section, we can further view this cross section as two cross sections in a parallel combination, in which the first has the vacuum below the metals, whereas the second has a finite-thickness dielectric substrate with relative permittivity $\varepsilon_r - 1$. We can then calculate the capacitance contributions from the vacuum and the substrate separately. We refer to the work [33] for an illustration of this separation.

The capacitance per unit length of the cross section with a vacuum below the metals can be calculated using the same conformal transformation function (23) as in the calculation of geometric inductance per unit length. Therefore, we have

$$C_l^{b,\text{vac}} = \varepsilon_0 \frac{W_b^{\text{vac}}}{H_b^{\text{vac}}} = 2\varepsilon_0 \frac{K(k_1)}{K(k_1')}. \tag{27}$$

For the cross section having a finite-thickness substrate with relative permittivity $\varepsilon_r - 1$, we can first do an intermediate transformation such that the substrate becomes infinitely thick to resemble the vacuum case above. We map the cross section from the z-plane to the t-plane with function

$$t(z) = \sinh\left[\frac{\pi z}{2h_b}\right]. \tag{28}$$

From the t-plane, we repeat the same Christoffel–Schwartz transformation but replace the variable notations in (23) from z to t. Fig. 8 shows the two consecutive conformal transformations.

Thus, we obtain

$$C_l^{b,\text{sub}} = (\varepsilon_r - 1)\varepsilon_0 \frac{W_b^{\text{sub}}}{H_b^{\text{sub}}} = 2(\varepsilon_r - 1)\varepsilon_0 \frac{K(k_2)}{K(k_2')} \tag{29}$$

with modules

$$k_2 = t_D/t_E = \sinh\left[\frac{\pi z_D}{2h_b}\right] / \sinh\left[\frac{\pi z_E}{2h_b}\right] = \sinh\left[\frac{\pi w_r}{4h_b}\right] / \sinh\left[\frac{\pi (w_r + 2s_r)}{4h_b}\right] \tag{30}$$

$$k_2' = \sqrt{1 - k_2^2}. \tag{31}$$

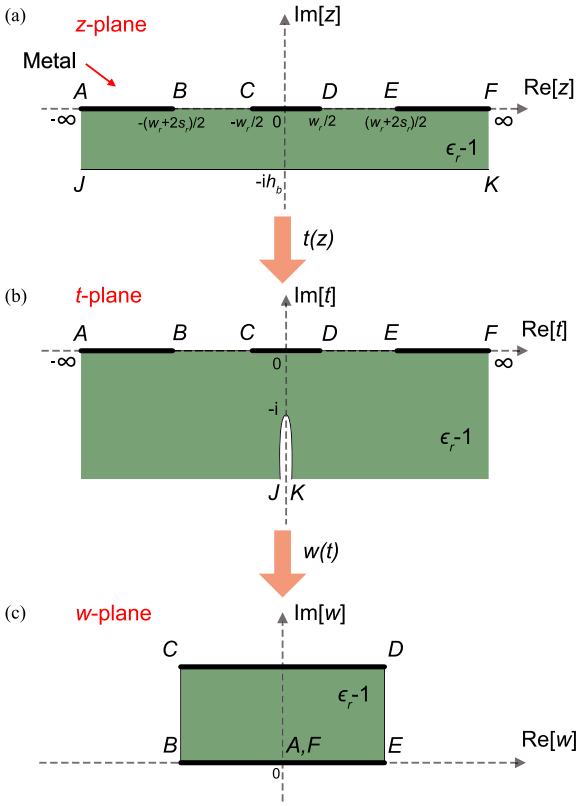

FIGURE 8. Conformal transformations for the bottom half of the flip-chip CPW cross-section when the substrate has relative permittivity $\varepsilon_r - 1$. (a) Original geometry. (b) Intermediate geometry in the t-plane. (c) Mapped to a parallel-plate waveguide.

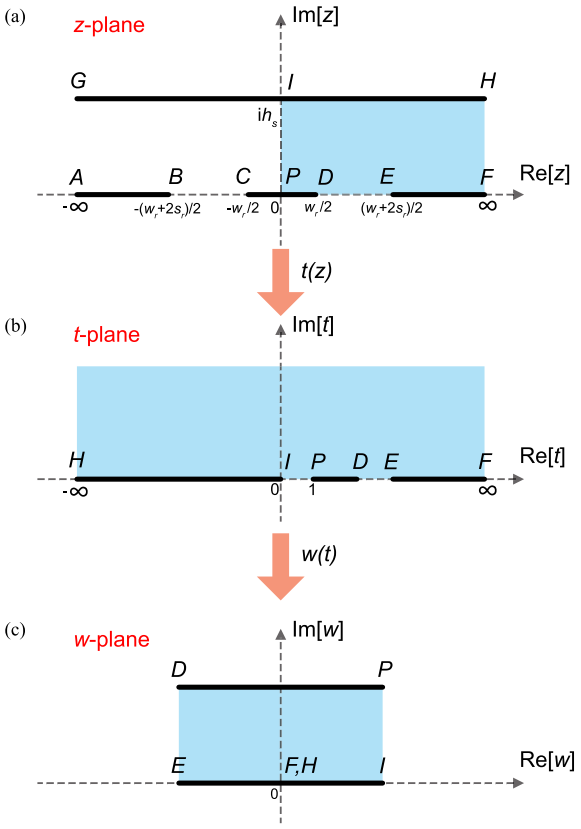

FIGURE 9. Conformal transformations for the top half of the flip-chip CPW cross-section. The transformed region is painted in cyan. (a) Original geometry. (b) Intermediate geometry in the t-plane. (c) Mapped to a parallel-plate waveguide.

Therefore, the geometric inductance and capacitance per unit length of the bottom half of the CPW cross-section are

$$L_l^{g,b} = \frac{\mu_0}{2}\frac{K(k_1')}{K(k_1)} \tag{32}$$

$$C_l^b = C_l^{b,\text{air}} + C_l^{b,\text{sub}} = 2\varepsilon_0\left[\frac{K(k_1)}{K(k_1')} + (\varepsilon_r - 1)\frac{K(k_2)}{K(k_2')}\right]. \tag{33}$$

B. TOP HALF

The top half of the CPW cross-section will be treated differently compared to the bottom half, as the top-half cross-section has a metal ground plane from the qubit tier on top of the CPW line. Since the qubit tier's metal ground plane blocks all the electromagnetic field generated from the CPW line, we can view the qubit tier's substrate as absent and replace it with vacuum.

To simplify the calculation, we exploit the symmetry of the top-half cross-section and only calculate the geometric inductance and capacitance per unit length of the cross section at the z-plane's real positive part (zero position is at the center of CPWs center conductor). The resultant two identical parallel-plate waveguides mapped from the real positive and negative parts are also treated as a parallel combination.

We do two consecutive conformal transformations to map the real positive part of the top-half cross-section into a parallel-plate waveguide. We first map the qubit tier's half of the metal ground plane in the z-plane to the Re[t]-axis, and then use the Christoffel–Schwartz transformation to map the geometry to a parallel-plate waveguide in the w-plane [13]. Fig. 9 shows the two conformal transformations.

The first transformation function we use is

$$t(z) = \cosh^2\left[\frac{\pi z}{2h_b}\right]. \tag{34}$$

In the z-plane, we define $z_P = 0$, $z_I = ih_s$, $z_D = w_r/2$ and $z_E = (w_r + 2s_r)/2$. In the t-plane, these points are mapped into $t_P = 1$, $t_I = 0$, $t_D = \cosh^2[\pi w_r/4h_b]$ and $t_E = \cosh^2[\pi(w_r + 2s_r)/4h_b]$.

The second transformation function we use is

$$w(t) = A_1 F(\varphi, k_s) + A_2 \tag{35}$$

where $F(\varphi, k_s)$ is the elliptic integral of the first kind with

$$F(\varphi, k_s) = \int_0^{\sin\varphi} \frac{d\tau}{\sqrt{(1 - k_s^2\tau^2)(1 - \tau^2)}} \tag{36}$$

$$\sin\varphi = \sqrt{\frac{(t - t_E)t_D}{(t - t_D)t_E}} \tag{37}$$

$$k_s = \sqrt{\frac{t_E(t_D - t_P)}{t_D(t_E - t_P)}}$$
$$= \tanh\left[\frac{\pi w_r}{4h_s}\right] \Big/ \tanh\left[\frac{\pi(w_r + 2s_r)}{4h_s}\right]. \quad (38)$$

After the second transformation, the real positive part of the top-half cross-section is now mapped to a parallel-plate waveguide, with the width and the height

$$W_t = |w_I - w_E| = |A_1|K(k_s) \quad (39)$$
$$H_t = |w_P - w_I| = |A_1|K(k_s') \quad (40)$$

where we have used the relations

$$F\left(\frac{\pi}{2}, k_s\right) = K(k_s) \quad (41)$$
$$F\left(\arcsin\frac{1}{k_s}, k_s\right) = K(k_s) + iK(k_s') \quad (42)$$
$$k_s' = \sqrt{(1 - k_s^2)}. \quad (43)$$

After combining the same results from the real negative part of the top-half cross-section, the geometric inductance and capacitance per unit length of the top half of the CPW cross-section are

$$L_l^{g,t} = \frac{\mu_0}{2}\frac{H_t}{W_t} = \frac{\mu_0}{2}\frac{K(k_s')}{K(k_s)} \quad (44)$$
$$C_l^t = 2\varepsilon_0\frac{W_t}{H_t} = 2\varepsilon_0\frac{K(k_s)}{K(k_s')}. \quad (45)$$

Therefore, the total geometric inductance and capacitance per unit length of the CPW cross-section in flip-chip geometry, when the CPW faces a metal ground plane on the opposing chip, are given in (2) and (3) in the main text.

APPENDIX B
EXTRACTION OF MAGNETIC PENETRATION DEPTH

To determine the magnetic penetration depth λ_m of our superconducting films, we compare 3-D-simulated and measured resonator frequencies (this time from single-chip devices, not flip-chip). We use L_l^k as a fitting parameter to account for the discrepancy between measured and simulated frequencies, since the model uses 2-D sheets with a perfect-E boundary condition, which does not include KI.

We measured six resonators on each of seven identical chips, see Fig. 10. We simulated the supercurrent density J_z in COMSOL [18]. We write the permittivity of the film as

$$\varepsilon_{\text{metal}} = \varepsilon_0 - \frac{1}{\omega^2\mu_0\lambda_m^2} \quad (46)$$

where $\omega = 2\pi f$ and $f = 6.6$ GHz is the frequency of the alternating current. The imaginary term of $\varepsilon_{\text{metal}}$ is negligible.

We obtain $\lambda_m = 83$ nm for our 150-nm-thick aluminum film. This is somewhat larger than the literature value of 50 nm [34], [35], suggesting that our film is in the dirty limit, with a mean free path smaller than the film thickness [19], [22], [36].

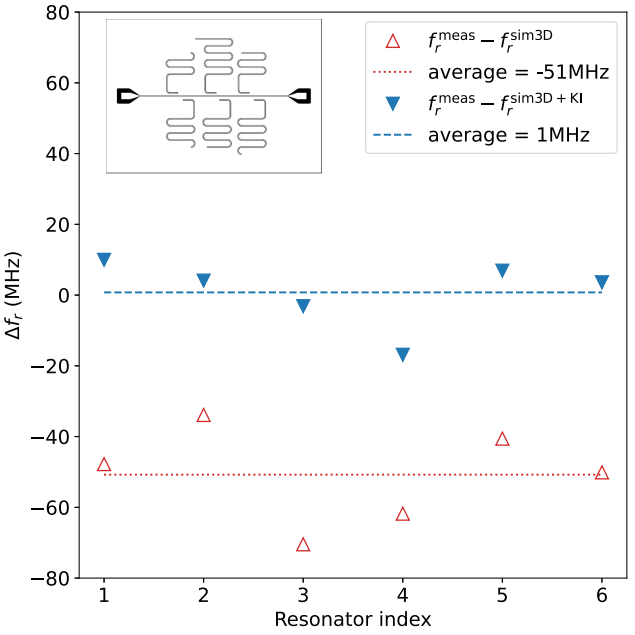

FIGURE 10. Difference between simulated and measured resonator frequencies. Each point represents the average of seven nominally identical resonators on different chips (single-chip, not flip-chip). The blue, downward-pointing triangles include the correction from KI, whereas the red, upward-pointing triangles do not. The inset shows the chip design with $w_r = 20\,\mu$m, $g_r = 10\,\mu$m.

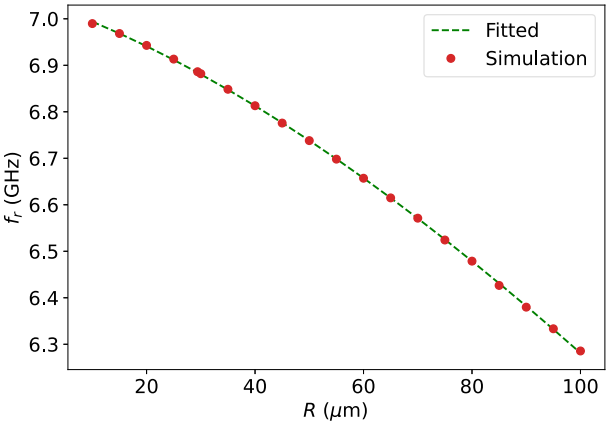

FIGURE 11. Decreasing resonator frequency f_r due to the increase of the radius R, i.e., the increase in the effective length of the circular coupling structure.

APPENDIX C
EFFECTIVE LENGTH DUE TO CIRCULAR COUPLING STRUCTURE

In order to determine the effective length of the circular resonator-qubit coupling pad shown in Fig. 1(b), we compare the resonator frequency from 3-D FEM simulation with

$$f_r = \frac{\beta}{l_r + \alpha_1 R^2 + \alpha_2 R}. \quad (47)$$

Here, $\beta = 1/(4\sqrt{L_l^g C_l})$ is a fixed value for given w_r, s_r, h_s, h_b, and ε_r. Fig. 11 shows the simulated resonator frequency

versus the radius R of the coupling pad, for interchip spacing $h_s = 8\,\mu$m, and a fit to (48).

We obtain the fitted parameters $\alpha_1 = 0.032\,\mu\text{m}^{-1}$ and $\alpha_2 = 2.9$ at $l_r = 5056\,\mu$m. We use these fitted parameters to obtain the effective length at different l_r and h_s during f_r and Q_c calculations in the main text. Repeated simulations at different l_r show that the change of calculated effective length ($\alpha_1 R^2 + \alpha_2 R$) at a given R is less than 3%.

We also repeat the simulations at different h_s, from 1 μm to 60 μm, and find that for our maximum investigated $R = 100\,\mu$m, the change of the calculated effective length, is less than 113 μm (18%), compared to its value for $h_s = 8\,\mu$m. Smaller R gives a smaller change, and we see that the change is kept at this value when $h_s \to \infty$. With $l_r = 5056.4\,\mu$m, the corresponding change of the resonator's frequency is less than 2%.

APPENDIX D
COMPUTATIONAL RESOURCES REQUIRED BY 2-D AND 3-D FEM SIMULATION

In this appendix, we show the comparison of required computational resources between 2-D and 3-D FEM simulations.

We did 3-D FEM simulations [26] of 25 resonators shown in Fig. 5(a). We use the same setting as in [5] with *Maximum Delta Frequency Per Pass* of 0.1% for the Eigenmode solver, and *Maximum Delta S* of 0.02 for the Driven Model solver. Across 25 resonators, the average spent CPU time was 32 h, and maximal memory allocation during Eigenmode simulation was 58 GB.

We conducted 2D FEM simulations [11] of the flip-chip CPW cross-section with interchip spacing h_s from 7 to 9 μm and step 0.2 μm. We use a *Percentage error* of 0.01% for both parameter convergence criteria *C only* and *L only*. The average spent CPU time was 1.7 min, and maximal memory allocation was 64 MB. Compared to 3-D FEM simulations, the CPU time and memory allocation were reduced by a factor of 1000 at each simulation.

In addition, we have also documented the used computational resources in COMSOL when simulating J_z over the metal thin films, with h_s from 7 to 9 μm with step 0.1 μm. The average solution time was 33 s and the allocated memory was 7.5 GB.

APPENDIX E
CROSS-SECTIONAL *Q*-FACTOR RESULTING FROM LOSSY DIELECTRIC INTERFACES

In this appendix, we calculate the Q-factor Q_{pr} of the resonator's CPW line cross-section in flip-chip architecture, based on the simulated participation ratio of different domains [37]. We use a similar 2-D FEM simulation setting as that in [5], with relative permittivities (4,4,7), loss tangents $(10^{-3}, 10^{-3}, 10^{-3})$, and film thicknesses $(2, 0.5, 2)$ nm for the substrate–air, substrate–metal, and metal–air dielectric interfaces in the simulation. Other geometry parameters of the CPW line cross-section are the same as in Section II when comparing conformal mapping techniques with 2-D FEM simulation.

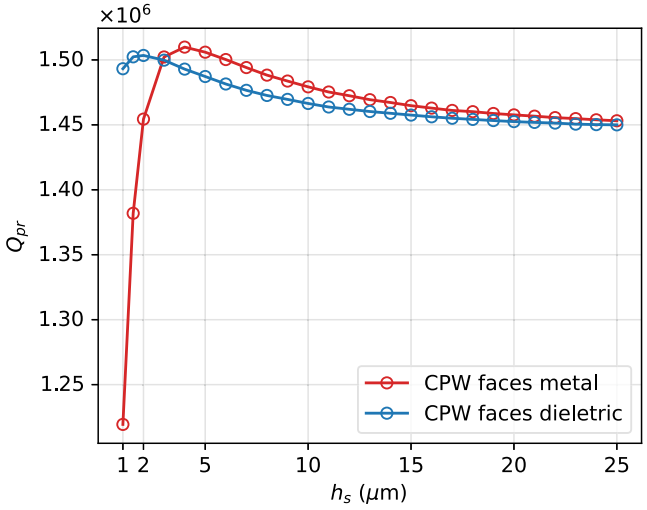

FIGURE 12. Cross-sectional *Q*-factor when the resonator's CPW line faces either the metal ground plane or the dielectric substrate of the qubit tier under different interchip spacings h_s.

The Q-factor Q_{pr} is calculated using

$$1/Q_{pr} = \sum_i p_i \tan\delta_i \tag{48}$$

where p_i is the simulated participation ratio for each domain i and $\tan\delta_i$ is the domain's loss tangent.

Fig. 12 shows the comparison of Q_{pr} between the resonator's CPW line facing either the metal ground plane or the dielectric substrate of the qubit tier under different interchip spacings h_s. As h_s decreases, there is a small increase of Q_{pr} until h_s is below a certain threshold. We also notice that Q_{pr} is slightly lower when the CPW line is facing a dielectric substrate on the qubit tier. The Q-factor drops significantly in the case when the resonator CPW line is facing metal, which is caused by the increased electric field strength inside the metal–air dielectric interfaces when h_s is very small [5].

ACKNOWLEDGMENT

The authors would like to thank Martí Gutierrez Latorre for his support on supercurrent density simulation in COMSOL. The authors are also grateful for discussions with David Niepce, Liangyu Chen, Janka Biznárová, Emil Rehnman, Christopher Warren, Anita Fadavi Roudsari, and Per Delsing, and technical assistance with cryogenics from Alexey Zadorozhko and Liangyu Chen. Author contributions: Hang-Xi Li conducted the analytical calculations, the numerical simulations, and the writing of the article. Daryoush Shiri provided critical inputs on the analytical calculations and supervised the work. Daryoush Shiri, Hang-Xi Li, and Sandoko Kosen developed the idea of interchip-spacing insensitive flip-chip resonator design. Sandoko Kosen and Hang-Xi Li designed the multiqubit flip-chip-integrated quantum processor. Marcus Rommel, Sandoko Kosen, Andreas Nylander,

and Hang-Xi Li fabricated the two chips of the processor at Chalmers, followed by Marco Caputo, Kestutis Grigoras, and Leif Grönberg conducting flip-chip bonding and gap measurements at VTT. Robert Rehammar, Giovanna Tancredi, and Sandoko Kosen provided the package of the processor and gave design advice on the processor's interface to the package. Hang-Xi Li and Sandoko Kosen measured the flip-chip resonators within the processor. Lert Chayanun fabricated and measured the single-chip resonators. Joonas Govenius supervised the work at VTT. Jonas Bylander supervised the whole work at Chalmers. The authors acknowledge the use of support and resources from Myfab Chalmers, and Chalmers Center for Computational Science and Engineering (C3SE, partially funded by the Swedish Research Council under Grant 2018-05973).

REFERENCES

[1] D. Rosenberg et al., "3D integrated superconducting qubits," *npj Quantum Inf.*, vol. 3, no. 1, Oct. 2017, Art. no. 42, doi: 10.1038/s41534-017-0044-0.

[2] B. Foxen et al., "Qubit compatible superconducting interconnects," *Quantum Sci. Technol.*, vol. 3, no. 1, Jan. 2018, Art. no. 0014005, doi: 10.1088/2058-9565/aa94fc.

[3] F. Arute et al., "Quantum supremacy using a programmable superconducting processor," *Nature*, vol. 574, no. 7779, pp. 505–510, Oct. 2019, doi: 10.1038/s41586-019-1666-5.

[4] P. Jurcevic et al., "Demonstration of quantum volume 64 on a superconducting quantum computing system," *Quantum Sci. Technol.*, vol. 6, no. 2, Apr. 2021, Art. no. 025020, doi: 10.1088/2058-9565/abe519.

[5] S. Kosen et al., "Building blocks of a flip-chip integrated superconducting quantum processor," *Quantum Sci. Technol.*, vol. 7, no. 3, Jul. 2022, Art. no. 035018, doi: 10.1088/2058-9565/ac734b.

[6] R. Acharya et al., "Suppressing quantum errors by scaling a surface code logical qubit," *Nature*, vol. 614, no. 7949, pp. 676–681, Feb. 2023, doi: 10.1038/s41586-022-05434-1.

[7] X. Zhang et al., "Digital quantum simulation of Floquet symmetry-protected topological phases," *Nature*, vol. 607, no. 7919, pp. 468–473, Jul. 2022, doi: 10.1038/S41586-022-04854-3.

[8] P. Zhang et al., "Many-body Hilbert space scarring on a superconducting processor," *Nature Phys.*, vol. 19, no. 1, pp. 120–125, Jan. 2023, doi: 10.1038/s41567-022-01784-9.

[9] Y. Kim et al., "Evidence for the utility of quantum computing before fault tolerance," *Nature*, vol. 618, no. 7965, pp. 500–505, Jun. 2023, doi: 10.1038/s41586-023-06096-3.

[10] R. Schinzinger and P. A. A. Laura, *Conformal Mapping: Methods and Applications*. New York, NY, USA: Dover Publications, 2003.

[11] "Ansys electronic desktop," 2D Extractor, Release, R1, 2020.

[12] G. Ghione and C. Naldi, "Coplanar waveguides for MMIC applications: Effect of upper shielding, conductor backing, finite-extent ground planes, and line-to-line coupling," *IEEE Trans. Microw. Theory Techn.*, vol. TMTT-35, no. 3, pp. 260–267, Mar. 1987, doi: 10.1109/TMTT.1987.1133637.

[13] S. Gevorgian, L. Linner, and E. Kollberg, "CAD models for shielded multilayered CPW," *IEEE Trans. Microw. Theory Techn.*, vol. 43, no. 4, pp. 772–779, Apr. 1995, doi: 10.1109/22.375223.

[14] J. Krupka, J. Breeze, A. Centeno, N. Alford, T. Claussen, and L. Jensen, "Measurements of permittivity, dielectric loss tangent, and resistivity of float-zone silicon at microwave frequencies," *IEEE Trans. Microw. Theory Techn.*, vol. 54, no. 11, pp. 3995–4001, Nov. 2006, doi: 10.1109/TMTT.2006.883655.

[15] K. L. Kaiser, *Electromagnetic Compatibility Handbook* (Electrical Engineering Handbook Series). Boca Raton, FL, USA: CRC, 2004.

[16] K. Yoshida, M. S. Hossain, T. Kisu, K. Enpuku, and K. Yamafuji, "Modeling of kinetic-inductance coplanar striplin with NbN thin films," *Jpn. J. Appl. Phys.*, vol. 31, pp. 3844–3850, Dec. 1992, doi: 10.1143/JJAP.31.3844.

[17] M. H. Amini, Z. Davoodi-Rad, A. Ghasemi, M. Khaliliy, and A. Mallahzadeh, "Current distribution and kinetic inductance of coplanar waveguide transmission lines," *IEEE Trans. Appl. Supercond.*, vol. 32, no. 8, Nov. 2022, Art. no. 3500606, doi: 10.1109/TASC.2022.3203029.

[18] D. Niepce, J. J. Burnett, M. G. Latorre, and J. Bylander, "Geometric scaling of two-level-system loss in superconducting resonators," *Supercond. Sci. Technol.*, vol. 33, no. 2, Jan. 2020, Art. no. 025013, doi: 10.1088/1361-6668/ab6179.

[19] P. B. Miller, "Penetration depth in impure superconductors," *Phys. Rev.*, vol. 113, no. 5, pp. 1209–1212, 1959, doi: 10.1103/PhysRev.113.1209.

[20] P. M. Tedrow, G. Faraci, and R. Meservey, "Measurement of the surface inductance and penetration depth of superconducting aluminum," *Phys. Rev. B*, vol. 4, no. 1, pp. 74–82, Jul. 1971, doi: 10.1103/PhysRevB.4.74.

[21] R. W. Cohen and B. Abeles, "Superconductivity in granular aluminum films," *Phys. Rev.*, vol. 168, no. 2, pp. 444–450, Apr. 1968, doi: 10.1103/PhysRev.168.444.

[22] M. Dressel, "Electrodynamics of metallic superconductors," *Adv. Condens. Matter Phys.*, vol. 2013, pp. 1–25, 2013, doi: 10.1155/2013/104379.

[23] P. Mangin and R. Kahn, *Superconductivity: An Introduction*. Cham, Switzerland: Springer, 2017, doi: 10.1007/978-3-319-50527-5.

[24] A. Blais, A. L. Grimsmo, S. Girvin, and A. Wallraff, "Circuit quantum electrodynamics," *Rev. Mod. Phys.*, vol. 93, no. 2, May 2021, Art. no. 025005, doi: 10.1103/RevModPhys.93.025005.

[25] I. Besedin and A. P. Menushenkov, "Quality factor of a transmission line coupled coplanar waveguide resonator," *EPJ Quantum Technol.*, vol. 5, no. 1, Dec. 2018, Art. no. 2, doi: 10.1140/epjqt/s40507-018-0066-3.

[26] "ANSYS electronic desktop," HFSS, Release, R1, 2020.

[27] R. N. Simons, *Coplanar Waveguide Circuits, Components, and Systems* (Wiley Series in Microwave and Optical Engineering Series). New York, NY, USA: Wiley, Mar. 2001, doi: 10.1002/0471224758.

[28] J. Heinsoo et al., "Rapid high-fidelity multiplexed readout of superconducting qubits," *Phys. Rev. Appl.*, vol. 10, no. 3, Sep. 2018, Art. no. 034040, doi: 10.1103/PhysRevApplied.10.034040.

[29] L. Chen et al., "Transmon qubit readout fidelity at the threshold for quantum error correction without a quantum-limited amplifier," *npj Quantum Inf.*, vol. 9, no. 1, Mar. 2023, Art. no. 26, doi: 10.1038/s41534-023-00689-6.

[30] M. Boissonneault, J. M. Gambetta, and A. Blais, "Improved superconducting qubit readout by qubit-induced nonlinearities," *Phys. Rev. Lett.*, vol. 105, no. 10, Sep. 2010, Art. no. 100504, doi: 10.1103/PhysRevLett.105.100504.

[31] G. Ghione and M. Goano, "Revisiting the partial-capacitance approach to the analysis of coplanar transmission lines on multilayered substrates," *IEEE Trans. Microw. Theory Techn.*, vol. 51, no. 9, pp. 2007–2014, Sep. 2003, doi: 10.1109/TMTT.2003.815873.

[32] C. Wen, "Coplanar waveguide: A surface strip transmission line suitable for nonreciprocal gyromagnetic device applications," *IEEE Trans. Microw. Theory Techn.*, vol. TMTT-17, no. 12, pp. 1087–1090, Dec. 1969, doi: 10.1109/TMTT.1969.1127105.

[33] E. Carlsson and S. Gevorgian, "Conformal mapping of the field and charge distributions in multilayered substrate CPWs," *IEEE Trans. Microw. Theory Techn.*, vol. 47, no. 8, pp. 1544–1552, Aug. 1999, doi: 10.1109/22.780407.

[34] T. P. Orlando and K. A. Delin, *Foundations of Applied Superconductivity*. Reading, MA, USA: Addison-Wesley, 1991.

[35] R. J. C. Charles, P. Poole, Jr., and A. H. Farach, *Superconductivity*. New York, NY, USA: Elsevier, 2007, doi: 10.1016/B978-0-12-088761-3.X5021-2.

[36] A. I. Gubin, K. S. Il'in, S. A. Vitusevich, M. Siegel, and N. Klein, "Dependence of magnetic penetration depth on the thickness of superconducting Nb thin films," *Phys. Rev. B.—Condens. Matter Mater. Phys.*, vol. 72, no. 6, pp. 1–8, 2005, doi: 10.1103/PhysRevB.72.064503.

[37] J. Wenner et al., "Surface loss simulations of superconducting coplanar waveguide resonators," *Appl. Phys. Lett.*, vol. 99, no. 11, Sep. 2011, Art. no. 113513, doi: 10.1063/1.3637047.